SiF 2026 – The 14th International Conference on Structures in Fire
Queen's University/ York University, Canada, 18 – 21 May 2026

AN INVESTIGATION OF EXPLOSIVE SPALLING IN CONCRETE: IS PORE PRESSURE MORE IMPORTANT OR THERMALLY INDUCED STRESS

Yunke Huang[1,*], Ming Chun Wong[2], Shuai Zhang[3], Liming Jiang[4], Asif Usmani[5]

ABSTRACT

Concrete spalling under fire critically threatens structural safety. It is widely attributed to coupled thermo-hygro-mechanical (THM) processes, but the relative roles of pore pressure and thermal stress remain disputed. This study addresses the issue by combining a fully coupled peridynamic THM model with H-TRIS fire tests on concrete slabs. The peridynamic framework couples heat, moisture and solid deformation with temperature-dependent permeability and damage, and introduce a volume-averaged damage metric to separate pore-pressure-driven and stress-driven contributions. Three-dimensional simulations directly reproduce crack initiation, propagation and spalling depth. H-TRIS tests with systematically varied water–cement ratio, in-plane restraint and polypropylene fibres show that high w/c and strong restraint produce the most violent spalling, while fibres largely suppress explosive cover loss. The simulations capture these trends and the observed damage morphologies. We found that for low-w/c concrete (w/c=0.3), damage and spalling is controlled by thermally induced stresses, particularly under rigid in-plane restraint. For high-w/c concrete (w/c=0.6), pore-pressure loading makes a substantial, though not dominant, contribution to damage, leading to distributed microcracking that relieves pressure without violent fragment ejection. The combined experimental–numerical framework clarifies spalling mechanisms and enables physics-based prediction of fire-induced concrete failure.

Keywords: Concrete structures; explosive spalling; peridynamic simulation; fire tests

1 INTRODUCTION

Concrete performance degrades catastrophically when exposed to the extreme temperatures of a fire, and explosive spalling is among the most critical failure modes. This violent process involves the rapid ejection of fragments at high velocity, abruptly reducing the structural cross section and exposing embedded reinforcement to temperatures exceeding 800°C. The resulting loss of load-bearing capacity can trigger progressive collapse, posing a severe threat to life safety and structural integrity in settings ranging from buildings to tunnels. The catastrophic nature of spalling is induced from the intricate interplay of thermal, hygral, and mechanical processes within the heated, porous concrete matrix. Design practice for critical structures remains largely

[1] Research Assistant Professor, The Hong Kong Polytechnic University
e-mail: yunke.huang@polyu.edu.hk, ORCID: https://orcid.org/0000-0002-9114-8267
[2] MSc student, The Hong Kong Polytechnic University
e-mail: ming-chun.wong@connect.polyu.hk, ORCID: https://orcid.org/0009-0008-0110-0712
[3] Research Assistant Professor, The Hong Kong Polytechnic University
e-mail: shuai-zs.zhang@polyu.edu.hk, ORCID: https://orcid.org/0000-0003-2750-114X
[4] Associate Professor, The Hong Kong Polytechnic University
e-mail: liming.jiang@polyu.edu.hk, ORCID: https://orcid.org/0000-0001-8112-2330
[5] Professor, The Hong Kong Polytechnic University
e-mail: asif.usmani@polyu.edu.hk, ORCID: https://orcid.org/0000-0003-2454-5737

prescriptive and based on standardized fire curves which are different from real fire scenarios, and more fundamentally, fail to capture the physics governing spalling initiation and progression.

Extensive experimental research on small to intermediate scale specimens reflected spalling characteristics, such as fragment size, velocity, and patterns under varying heating rates, moisture contents, and mix designs [1-3]. Influential factors include polypropylene fibres, water–cement ratio, aggregate type, and external mechanical restraint [4]. It is broad recognition that explosive spalling in fire-exposed concrete originates from coupled thermo-hygro-mechanical (THM) processes. When heating is rapid, as in tunnel fires, the combined action of thermally induced stresses and rising pore vapour pressure can overcome the tensile strength of the material [5,6]. Although the underlying physics of heat and moisture transport in porous media were established decades ago, the precise contribution of each driving mechanism remains contested. The debate focused on a question: whether pore pressure buildup or thermally induced stress is the primary trigger for spalling [7]. This question remains unsolved because conventional constitutive models and one-way coupling strategies cannot adequately resolve the dynamic interplay between these mechanisms, and therefore fail to inform robust, physics-based design solutions [8].

Numerical modelling has become essential tool for studying the multi-physics nature of concrete spalling by revealing internal fields variations, such as pore pressure evolution and stress redistribution that are difficult to measure experimentally. Early finite element (FE) formulations, including the thermo-hygral model proposed by Bažant and Thonguthai [9], simplified moisture transport in a simplified manner. Later work extended this to fully coupled thermo-hygro-mechanical (THM) models, which explicitly link pore pressure evolution to skeleton deformation [10]. More recent efforts have incorporated chemical degradation from dehydration, giving rise to chemo-hygro-thermal-mechanical (CHTM) frameworks [11]. However, continuum-based FE methods face inherent limitations when simulating explosive spalling. The process involves highly discontinuous, dynamic fracture with spontaneous crack initiation, branching, and fragmentation. Standard formulations that rely on ad-hoc failure criteria or element deletion without a clear physical basis face challenge when displacement discontinuities appear. The local nature makes it difficult to represent multi-scale effects, and complex crack interactions that govern concrete fracture under fire. Peridynamics (PD), a nonlocal reformulation of continuum mechanics, offers a promising alternative. The meshless, particle-based formulation replaces spatial derivatives with spatial integrals that remain valid across discontinuities, allowing spontaneous formation and propagation of complex crack patterns without auxiliary failure criteria [12]. Peridynamic formulations have been extended to thermal diffusion and thermo-mechanical problems [13], and initial progress has been made for poroelastic media and early-age concrete [14]. However, application of PD to fully coupled THM modelling of fire-induced spalling is still at an early stage [15]. In particular, a significant gap exists in incorporating dynamic moisture transport, pore-pressure evolution, and their explicit interaction with fracture within a unified PD framework.

Evaluating the dominant reason that drives explosive spalling requires a methodology that links coupled physical processes with material failure. This study tackles that problem by developing a fully coupled peridynamic THM numerical model and a strategically designed experimental program. Our contributions are as follows. First, a comprehensive PD-THM framework that fully couples thermal, hygral, and mechanical fields with damage evolution is established to capture the progression from initial damage to fragmentation. Second, a numerical mechanism isolation strategy is implemented within this framework to quantitatively assess the individual contributions of thermal stress and pore pressure to failure using three-dimensional PD-THM simulations of slabs subjected to heat flux. Third, a series of controlled fire tests on concrete slabs are conducted with varied restraint conditions, polypropylene fibre contents and water–cement ratios, providing independent mechanistic insight and essential validation data. By combining high-fidelity simulation of spontaneous cracking with targeted experimentation, this research aims to clarify the dominant spalling mechanisms over a range of conditions and to establish a physics-based framework for assessing the fire resilience of concrete.

2 MODEL OF THERMO-HYGRO-MECHNICAL COUPLED PERIDYNAMICS

2.1 Peridynamic Formulation for Heat Conduction

Peridynamics is a non-local computational theory originally formulated by Silling et al. [12]. Within this framework, a material point **x** interacts with other points in its vicinity. These neighboring points, referred as family points **x'**, lie within a finite region of influence, known as the horizon. The horizon, , with a radius , defines the maximum separation distance for interactions, as shown in Figure 1(a). In peridynamics, the connection between a point **x** and its family member **x'** is defined as a “bond”. Each bond is governed by response functions, which contains the constitutive information corresponding to the material point **x**. Interactions beyond the horizon radius are considered negligible. In peridynamic thermal diffusion, the material point **x** is connected to its neighboring point **x'** through a temperature bond. The thermal diffusion equation in PD can be represented as [16]:

$$\rho c_V\left(T\right)\frac{\partial T\left(\mathbf{x},t\right)}{\partial t}=\int_{H_{\mathbf{x}}} f_T\left(T',T,\mathbf{x}',\mathbf{x},t\right)dV_{\mathbf{x}'}+h_s\left(\mathbf{x},t\right) \tag{1}$$

where represents the mass density of object, represents the specific heat capacity, represents the volume of **x'**, and and denote the temperatures of **x'** and **x**, respectively. The heat source density indicates the heat generated by the heat source per unit volume. The thermal response function, , is defined as the thermal interaction between material particles **x** and **x'**, which can be expressed as:

$$f_T\left(T',T,\mathbf{x}',\mathbf{x},t\right)=\kappa_{micro}\frac{T'-T}{\left|\xi\right|} \tag{2}$$

where ξ= **x'- x** is the relative position vector between material point **x'** and **x**. The microthermal conductivity for PD formula is denoted by κ_{micro}, and can be calculated as $6k/(\pi h\delta^3)$ and $6k/(\pi\delta^4)$ for 2-D and 3-D model respectively, with k denotes the thermal conductivity, and h is the model thickness.

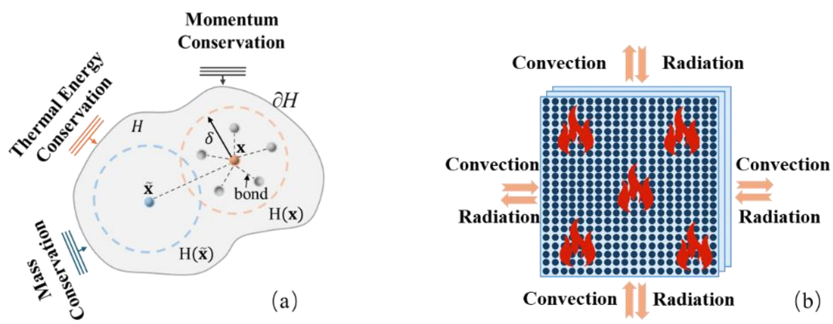

Figure 1. (a) Illustration of the PD-THM framework; (b) Model configuration for the PD simulation of a concrete slab under fire.

2.2 Peridynamic Formulation for Pore Pressure Evolution

The violent spalling of concrete under fire is generally attributed to the combined action of rapidly evolving pore pressure and thermally induced stresses. The contribution of pore pressure originates from the evaporation of pore water and subsequent expansion of the generated vapour. This process is intrinsically governed by the coupled evolution of two key field variables: the liquid-water saturation , representing the fraction of pore space occupied by liquid water, and the vapour partial pressure . Their evolution is driven by the temperature field and fundamentally coupled through phase change at the liquid–vapour interfaces. The thermodynamic potential for evaporation at any point is given by the local saturation vapour pressure, determined by temperature via a Clausius–Clapeyron-type relation as [10]

$$p_{sat}(T)=p_0\exp[\frac{\Delta H_{vap}}{R_v}\left(1/T-1/T_0\right)] \tag{3}$$

where $p_0 = 101325\text{Pa}$ at $T_0 = 373\text{K}$, $\Delta H_{vap} = 2.26\times10^6\,\text{J}\cdot\text{kg}^{-1}$ is the latent heat of evaporation per unit mass, and $R_v = 461.5\text{J}\cdot\text{kg}^{-1}\cdot\text{K}^{1}$ is the specific gas constant of water vapour. The actual rate of mass conversion from liquid to vapour depends on the departure from this equilibrium and on the amount of liquid available. The volumetric evaporation mass-transfer rate $\dot{m}_{evap}$ is proportional to the positive difference between the saturation pressure and the local vapour pressure and scaled by the liquid saturation as [10]:

$$\dot{m}_{evap} = k_{evap} S\phi \frac{1}{R_v T}(p_{sat}(T) - p_v)^+ \tag{4}$$

where $k_{evap} = 5.0\times10^6\,\text{m}\cdot\text{s}^{-1}$ is effective volumetric mass transfer coefficient, ϕ is the porosity, and $(p_{sat}(T) - p_v)^+$ denotes the positive part ensuring evaporation occurs only when $p_{sat} > p_v$.

The conservation of mass for the liquid-water phase, incorporating its transport through the porous medium, is classically described in terms of the saturation by a Richards-type equation:

$$\phi\frac{\partial S}{\partial t} = \nabla\cdot[D_h(S)\nabla S] - m_{evap}/\rho_l \tag{5}$$

where $D_h(S)$ is an effective hydraulic diffusivity and ρ_l is the liquid water density. This form corresponds to a Fickian approximation of liquid transport, with capillary pressure and gravity effects absorbed into . A representative value for the diffusivity of heated concrete can be specified as $D_h = 10^{-8}\,\text{m}^2\cdot\text{s}^{-1}$. In the peridynamic framework, the spatial gradient term is replaced by a non-local integral over the material horizon , yielding the PD saturation evolution equation as:

$$\frac{\partial S(\mathbf{x},t)}{\partial t} = \int_{\text{H}_x} \frac{D_h}{|\xi|^2}\left[S(\mathbf{x}',t) - S(\mathbf{x},t)\right]dV_{\mathbf{x}'} - \frac{\dot{m}_{\text{evap}}(\mathbf{x},t)}{\rho_l\phi} \tag{6}$$

Similarly, based on the conservation of mass for the vapour phase and Darcy's law, the classical nonlinear vapour-pressure diffusion equation with an effective pressure-diffusivity coefficient D_p can be derived by using standard simplifications of $S_g \approx 1$ and $1/R_v T$ is slowly varying in time as [10]:

$$\frac{\partial p_v}{\partial t} = \nabla\cdot\left[D_p\nabla^2 p_v\right] + \dot{m}_{evap}R_v T/\phi, \quad D_p = \frac{\kappa p_0}{\mu_g\phi} \tag{7}$$

with S_g is the gas saturation, $\rho_v = p_v/(R_v T)$ is the vapour density, κ is intrinsic permeability and μ_g is gas viscosity. Given $\kappa = 1.0\times10^{-16}\,\text{m}^2$, $\mu_g = 1.2\times10^{-5}\,\text{Pa}\cdot\text{s}$, $\phi = 0.12$ gives $D_p = 7.036\times10^{-6}\,\text{m}^2\text{s}^{-1}$.

Eq.(7) represents the mass flux converted into a pressure increase via the ideal gas law, and can be recast in the peridynamic form as:

$$\frac{\partial p_v(\mathbf{x},t)}{\partial t} = c_d\int_{\text{H}_\mathbf{x}} \frac{D_p}{|\xi|^2}[p_v(\mathbf{x}',t) - p_v(\mathbf{x},t)]dV_{x'} + m_{evap}(\mathbf{x},t)/R_v T(\mathbf{x},t) \tag{8}$$

where c_d is a horizon-dependent constant chosen as $9/\left(2\pi\delta^3\right)$ for three-dimension and $4/\left(\pi\delta^2\right)$ for two-dimension, such that the integral operator converges to $D_p\nabla^2 p_v$ in the limit of vanishing horizon.

2.3 Peridynamic Mechanical Formulation for Coupled THM Analysis

The mechanical response, cracking, and spalling are modelled using a three-dimensional non-ordinary state-based correspondence peridynamic formulation [12]. This framework offers a general and physically consistent framework for modeling materials with complex constitutive behavior, including the pressuredependent and temperature-sensitive response of concrete. For a material point $\mathbf{x}$ with horizon , the equation of motion is governed by:

$$\rho \ddot{\mathbf{u}}(\mathbf{x},t) = \int_{H_{\mathbf{x}}} \{\mathbf{T}[\mathbf{x},t] - \mathbf{T}[\mathbf{x}',t]\} dV_{\mathbf{x}'} + \mathbf{b}(\mathbf{x},t) \quad (9)$$

where $\ddot{\mathbf{u}}$ is the acceleration, is an external body force density field, and $\mathbf{T}[\mathbf{x},t]$ is the force state that operating on $\mathbf{x}$ by $\mathbf{x}'$. For non-local small strain tensor, the correspondence mapping from to the force state is taken as:

$$\mathbf{T}[\mathbf{x},t] = \omega\langle|\xi|\rangle \boldsymbol{\sigma}(\mathbf{x}) \mathbf{K}^{-1}(\mathbf{x}) \xi \quad (10)$$

where $\omega\langle|\xi|\rangle$ is the influence function, is the Cauchy stress, is the nonlocal shape tensor that can be defined by the product of the initial relative position vector state ξ as $\mathbf{K}(\mathbf{x}) = \int_{H_{\mathbf{x}}} \omega\langle|\xi|\rangle [\xi \otimes \xi] dV_{\mathbf{x}'}$.

For thermo-poroelastic mechanics, the Cauchy stress is introduced through Biot's concept by considering pore pressure induced volumetric effect as $\boldsymbol{\sigma} = \boldsymbol{\sigma}' - \alpha p_v \mathbf{I}$. Here $\boldsymbol{\sigma}'$ is the effective stress given by a linear elastic constitutive law as $\boldsymbol{\sigma}' = \mathbf{C} : (\boldsymbol{\varepsilon} - \boldsymbol{\varepsilon}_{\mathbf{th}})$ with C denotes the stiffness matrix, denotes the Biot coefficient, and denotes the identity tensor. For small strains, a symmetric nonlocal strain tensor is extracted as $\boldsymbol{\varepsilon} = \frac{1}{2}(\mathbf{F} + \mathbf{F}^T) - \mathbf{I}$ with a nonlocal deformation gradient $\mathbf{F}$ computed by current and reference bond vectors as $\mathbf{F} = \left[\int_{H_{\mathbf{x}}} \omega\langle|\xi|\rangle \mathbf{Y}\langle\xi\rangle \otimes \xi dV_{\mathbf{x}'} \right] \mathbf{K}^{-1}$ [12]. An isotropic thermal strain can be expressed as $\boldsymbol{\varepsilon}_{\mathbf{th}} = \alpha_T (T - T_0) \mathbf{I}$ with thermal expansion coefficient α_T, current temperature T and reference temperature T_0.

Damage evolution is governed by a local stretch-based criterion implemented at the peridynamic bond level. A scalar damage variable $\mu(\xi,t) \in [0,1]$ of a bond between two material points $\mathbf{x}$ and $\mathbf{x}'$ can be given as:

$$\mu(\xi,t) = \begin{cases} 1, & s - \tau \Delta P_{avg} - \alpha_T \Delta T_{avg} < s_{cr} \\ 0, & \text{otherwise} \end{cases} \quad (11)$$

with s_{cr} denotes the critical stretch [15]. The damage effect can be included in equation of motion by modifying the force state as $\mathbf{T}[\mathbf{x},t] = \mu(\xi,t) \cdot \left[\omega\langle|\xi|\rangle \boldsymbol{\sigma}(\mathbf{x}) \mathbf{K}^{-1}(\mathbf{x}) \xi \right]$. The peridynamic damage level of material point $\mathbf{x}$ at time t can be determined as:

$$\varphi(\mathbf{x},t) = 1 - \frac{\int_{H_{\mathbf{x}}} \mu(\xi,t) dV_{\mathbf{x}'}}{\int_{H_{\mathbf{x}}} dV_{\mathbf{x}'}} \quad (12)$$

For numerical implementation procedure, the coupled system of equations governing moisture transport, vapour pressure evolution, and mechanical failure is solved using an explicit time-marching scheme within the peridynamic framework. At each time step t^n, the fields T^n, S^n and p_v^n are known. The update to time $t^{n+1} = t^n + \Delta t$ proceeds sequentially, ensuring the physical coupling is respected. This force density vector is updated explicitly to the discrete linear momentum equation of the solid phase, and the mechanical fields of displacement and velocity can be subsequently performed using an explicit adaptive dynamic [16]. The explicit coupling requires that the time step satisfies stability conditions of hygro-diffusion processes $\Delta t < C \Delta x^2 / \max(D_h, D_p)$, with $C = 0.1$ and Δx for discretization interval. This explicitly coupled update strategy ensures a stable and physically consistent integration of the thermo-hygro-mechanical response leading to spalling.

3 NUMERICAL SIMULATION FOR CONCRETE SLAB SPALLING

3.1 Numerical case design and boundary conditions

The PD–THM model is used to simulate fire-induced damage in concrete slabs. The slabs have dimension of $300\text{mm} \times 300\text{mm} \times 40\text{mm}$. Two water–cement ratios are considered: a dense, low-permeability concrete of w/c ratio = 0.30 and a more porous, high-moisture concrete of w/c ratio = 0.60. The w/c ratio have direct effect on the elastic modulus, density, permeability, porosity and thermal conductivity. For each mix, two in-plane restraint conditions are modelled: a free configuration, where slab edges are unrestrained, and a framed configuration, where the perimeter is kinematically fixed to represent a rigid frame. This yields four configurations, (0.30, free), (0.30, framed), (0.60, free) and (0.60, framed). All slabs are subjected to a constant radiant heat flux of 140 kW/m² on the exposed face. The boundaries of unexposed faces are exposed to ambient air with heat transfer governed by both convection and radiation, as shown in Figure 1(b).

Within each configuration, three coupling levels are analysed to separate thermal-stress and pore-pressure effects. In the fully coupled THM simulations, heat transfer, moisture transport, pore-pressure evolution and solid deformation are solved in a unified PD framework. In thermo–mechanical (T–M) simulations, the same temperature field and temperature-dependent degradation are used, but pore-pressure loading is removed from the mechanical equations so that damage arises solely from thermal strains and high-temperature softening. In hygro–mechanical (H–M) simulations, temperature-driven moisture transport and pore-pressure loading is retained while thermal expansion is omitted. The discretization of $90 \times 90 \times 12$ and peridynamic horizon of $3.015\Delta x$ are fixed across all simulations. Consequently, differences in response reflect only the activated mechanisms. Comparing the THM, T-M, and H-M predictions for each configuration quantifies the individual and combined contributions of thermal stress and pore pressure.

3.2 Damage metric and mechanism isolation strategy

To compare the twelve simulations on a consistent basis, the overall damage level at the end of the fire exposure is quantified by a volume-averaged damage index

$$\bar{D} = \frac{1}{V_{tot}} \sum_i \varphi(\mathbf{x}_i, t) V_i \tag{13}$$

where $\varphi(\mathbf{x}_i, t)$ is the peridynamic damage variable of material point $\mathbf{x}_i$, V_i is its associated volume, and V_{tot} is the total slab volume. This scalar index measures the fraction of the slab volume that has undergone bond damage and serves as a proxy for spalling severity in the absence of explicit fragment tracking. For each w/c and restraint configuration, the three simulations yield $\bar{D}^{THM}$, $\bar{D}^{TM}$ and $\bar{D}^{HM}$. To learn the respective roles of thermal stress and pore pressure, two dimensionless indicators are introduced:

$$R_T = \frac{\bar{D}^{THM} - \bar{D}^{HM}}{\bar{D}^{THM}}, R_P = \frac{\bar{D}^{THM} - \bar{D}^{TM}}{\bar{D}^{THM}} \tag{14}$$

where R_T is the thermal-damage contribution ratio and measures the portion of the fully coupled THM damage that is attributed to thermally induced stresses. Conversely, R_P, the pore-pressure-damage contribution ratio, quantifies the complementary contribution of pore pressure beyond pure thermal loading.

3.3 Parametric trends and key findings from PD simulations

The PD–THM simulations reflect the main crack patterns and clarify how the relative importance of thermally induced stress and pore pressure varies with water–cement ratio and in-plane restraint. Figure 2(a) shows contour plots of the final damage field based on peridynamic damage level of material points for all four w/c–restraint combinations, each simulated under three coupling levels. Figure 2(b) summarizes these results into the volume-averaged damage index ^{M}, ^{M} and ^{M} for each case, while Figure 2(c) presents the corresponding thermal- and pore-pressure-damage contribution ratios, and .

For the low w/c concrete (w/c = 0.30), both free and restrained cases are characterised by relatively sparse but wide and deep cracks. Under free expansion, only a thin damaged band develops near the heated surface, with a few wide, deep cracks propagating into the slab depth and a low damage index ^{M}. When rigidly restrained, a small number of these cracks further widen and penetrate through the thickness, forming intersecting, through-thickness fracture paths. In contrast, the high w/c concrete (w/c = 0.60) exhibits a dense network of narrow, shallow cracks concentrated in a thicker surface layer. Compared with w/c = 0.30, ^{M} is higher for w/c = 0.60 due to the much more intensive though shallower cracking. Thus, lower w/c favours sparse, wide, and deep cracking, while higher w/c produces dense, shallow, and narrow cracking.

The three coupling levels isolate the relative roles of thermal stress and pore pressure. For w/c = 0.30, the T–M simulations reproduce both the extent and morphology of cracking obtained in the fully coupled THM simulations, whereas the H–M simulations show only minor, very shallow surface damage. The contribution ratios therefore satisfy , indicating that thermally induced stresses dominate damage in dense, low-permeability concrete and that pore pressure alone does not generate substantial cracking. For w/c = 0.60, the H–M simulations reproduce an increasing portion of the dense shallow crack network seen in the THM simulations. As a result, increases significantly compared with the low-w/c case, although it remains consistently smaller than . This shows that in high-w/c concrete, pore-pressure-driven loading makes a substantial but still secondary contribution to dense and shallow cracking pattern, while thermal stresses remain the dominant component and act increasingly as a localisation and amplification mechanism.

The influence of framed restraint is also clearly reflected in the simulations. For low-w/c slabs, adding rigid in-plane restraint transforms a thin near-surface damage zone with sparse wide cracks into a configuration with a few wide, deep, through-thickness fractures and a significantly increased ^{M} and ^{M}. This behaviour is governed by stress concentration under restrained thermal dilation and is captured almost entirely by the T–M simulations, reinforcing that stress-dominated damage controls potential explosive spalling in low-w/c concrete. For high-w/c slabs, the frame further increases ^{M} to the highest values among all cases and densifies the network of narrow, shallow cracks near the heated surface. The H–M simulations still account for an appreciable share of the THM damage, with increasing but consistently less than . This indicates that rigid restraint in high-w/c slabs mainly intensifies near-surface fragmentation rather than promoting extensive through-thickness failure.

Overall, the PD simulations show that low-w/c concrete tends to develop sparse, wide, deep cracks controlled by thermal stresses, particularly under rigid restraint, enabling explosive spalling. High-w/c concrete develops dense, narrow, shallow cracks driven by a combination of pore pressure and thermal stress, with pore pressure contribution is less then thermal contribution but increasing significantly compared with the low-w/c case, leading to pervasive but non-explosive damage.

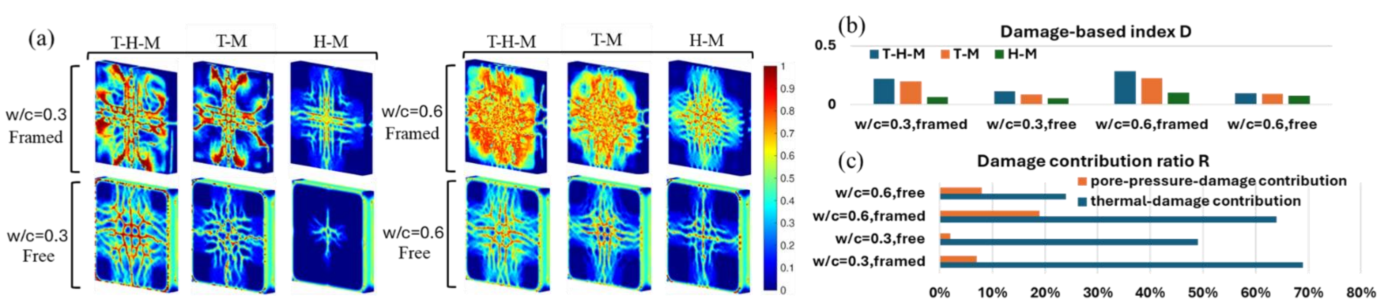

Figure 2 (a) Contour plot of damage field for all w/c–restraint combinations and coupling modes. (b) Damage index *D* for all w/c–restraint combinations and coupling modes. (c) Damage contribution ratio *R* for all w/c–restraint combinations.

4 EXPERIMANTAL PROGRAMM

4.1 H-TRIS calibration

The H-TRIS radiant system is fueled by two 21-L LPG gas cylinders to operate continuously for approximately 3–5 h. A radiant panel array of 300 mm × 400 mm is supplied at a regulated pressure of 200–250 kPa, ensuring stable combustion and a nearly constant incident heat flux on the concrete specimens during the tests. Heat flux gauges were used to measure the incident flux at different stand-off distances from the panel surface.

Calibration shows that the incident heat flux decreases with increasing stand-off distance, with a steep drop at short distances followed by a more gradual decay, characteristic of radiative attenuation rather than a linear trend. Flux fluctuations are larger closer to the panel and become more uniform with distance. A stand-off distance of 150 mm yields the maximum average heat flux of approximately 140 kW/m² while maintaining good spatial uniformity. This distance was therefore adopted for all spalling tests to provide a high, stable and reproducible thermal loading condition.

Table 1. Mix proportions and initial physical properties of concrete specimens.

Specimen	Water Ratio	18mm PP Fibre (kg)	Compress Strength (MPa)	Concrete Volume (m^3)	Total Mass (kg)	Prestressed Frame Mass (kg)	Concrete Mass (kg)	Concrete Density (kg/m^3)
A	0.3	0.007	70	0.0036	9.19	0.76	8.43	2341.667
B	0.3	0.007	70	0.0036	8.67	N.A.	8.67	2408.333
C	0.3	N.A.	70	0.0036	8.17	0.76	7.41	2058.333
D	0.3	N.A.	70	0.0036	9.02	N.A.	9.02	2505.556
E	0.6	0.007	30	0.0036	8.44	0.76	7.68	2133.333
F	0.6	0.007	30	0.0036	7.64	N.A.	7.64	2122.222
G	0.6	N.A.	30	0.0036	7.50	0.76	6.74	1872.222
H	0.6	N.A.	30	0.0036	8.17	N.A.	8.17	2269.444

4.2 Sample Preparation

The experimental programme was designed to isolate the effects of restraint, moisture/pore pressure and permeability on spalling. Eight concrete slabs were cast in three parameter groups: (i) with and without a rigid restraining steel frame, to assess the role of thermally induced in-plane stresses; (ii) with and without polypropylene (PP) fibres, to examine pore-pressure relief through melt-induced venting channels; and (iii) with water–cement ratios of 0.30 and 0.60, which jointly affect permeability and mechanical strength.

All mixes used Ordinary Portland Cement ASTM Type I, crushed granite (10–15 mm) as coarse aggregate and natural river sand as fine aggregate [17]. For the low w/c mix (0.30), 1% superplasticizer by cement mass was added to ensure workability without reducing strength. Selected slabs contained 18 mm PP fibres at the specified dosage. After casting, specimens were cured for 28 days. The 0.30 w/c ratio mix achieved a compressive strength of about 70 MPa, representing a high-strength, high-spalling-risk concrete, whereas the 0.60 w/c ratio mix reached approximately 30 MPa, representative of conventional-strength concrete. The summary of concrete specimen preparation is shown in Table 1.

4.3 Parametric trends and key findings from H-TRIS tests

The H-TRIS tests on eight slabs revealed consistent trends linking spalling probability and damage morphology to water–cement ratio, in-plane restraint and PP fibres, which are corroborated by the measured changes in mass, volume and density after heating. The H-TRIS test results are shown in Figure 3.

For the low w/c series (0.30), the unrestrained slab without PP fibres developed only shallow scaling and a sparse pattern of medium-to-wide surface cracks under an incident heat flux of approximately 140 kW/m². Its concrete density decreased by about 9 %, accompanied by a small volumetric expansion (~3%), indicating moderate internal damage dominated by near-surface cracking. When the same mix was tested within the rigid steel frame and without PP fibres, the damage became markedly more severe: only a few cracks formed, but they widened and deepened, coalesced through the thickness and led to sudden cover detachment, i.e. explosive spalling. This slab showed a comparable, intermediate density loss (~8%) with essentially negligible volumetric expansion, consistent with a stress-dominated failure in which restrained thermal dilation drives a limited number of through-thickness fractures rather than diffuse microcracking. This pairwise comparison isolates the effect of in-plane restraint and shows that, in dense low-w/c concrete, thermally induced stresses under restraint were the critical trigger for explosive spalling.

In contrast, the high w/c slabs (0.60) developed a much denser and more finely spaced crack network than the corresponding low w/c slabs under the same boundary conditions, irrespective of restraint. This is reflected in the generally higher or comparable density losses (≈8–11% in PP-fibre mixes) combined with small but positive volume changes (up to ~5%), indicating that internal damage was distributed over a network of fine cracks rather than concentrated in a few major fractures. The more intensive cracking reflects the higher moisture content and permeability of these mixes, which leads to rapid pore-pressure build-up and subsequent distributed microcracking. In all high w/c specimens, this microcracking and slight expansion were sufficient to relieve pore pressure, and no explosive spalling was observed.

PP fibres systematically modified both crack morphology and bulk property changes. Fibre-reinforced specimens exhibited finer and more evenly distributed cracks, while fibre-free slabs tended to develop fewer but wider cracks. For a given w/c and restraint condition, the presence of PP fibres promoted deeper but narrower cracking, consistent with a more gradual redistribution of pore pressure through an extended network of microcracks and melt-induced venting channels. This is in line with the larger density losses (≈10–15%) observed in the fibre-reinforced slabs, which reflect more pervasive internal damage without macroscopic fragment ejection. None of the fibre-reinforced slabs exhibited explosive spalling, whereas explosive cover loss occurred only in the low w/c (0.30) slab tested within the rigid frame without PP fibres.

The visual observations and post-fire measurements indicate that pore pressure governed the extent of distributed cracking in high w/c concrete and fibre-reinforced mixes, whereas thermally induced stresses under in-plane restraint governed the onset of explosive spalling in dense, low w/c concrete without fibres. The restraining frame intensified cracking in all cases, but only the combination of low w/c, rigid restraint and absence of fibres produced stress-dominated spalling. In all other cases, damage remained crack-dominated, with density loss controlled by diffuse microcracking and limited surface scaling rather than fragment ejection.

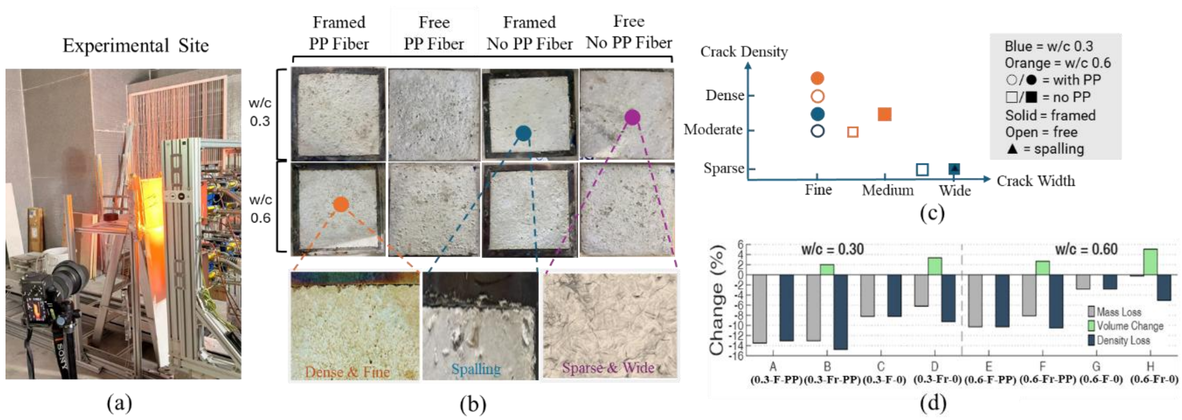

Figure 3 (a) Schematic of the H-TRIS radiant heating setup. (b) Post-fire photographs of the heated faces for all tested slabs. (c) Qualitative summary of crack density, crack width and spalling occurrence. (d) Post-fire changes in concrete mass, volume and density for all eight slabs.

5 CONCLUSION

This study integrated a fully coupled peridynamic thermo-hygro-mechanical (PD-THM) model with H-TRIS fire tests on concrete slabs to elucidate the roles of thermally induced stress and pore pressure in explosive spalling. The PD-THM framework successfully reproduced observed crack patterns and enabled quantitative evaluation of damage contributions through mechanism isolation. The H-TRIS tests showed that only low w/c ratio concrete without PP fibres under rigid in-plane restraint experienced explosive cover loss, while all other configurations exhibited non-explosive and crack-dominated damage. Consistently, the simulations indicated that in low w/c ratio concrete damage is governed by thermally induced stresses with restraint essential for through-thickness fracture. In high w/c ratio concrete, pore pressure was numerically observed to make a substantial contribution by generating dense shallow cracking, which is consistent with test observation. PP fibres were shown experimentally to promote distributed microcracking, thereby suppressing explosive spalling by pressure relief. Although limited to plain concrete under radiant heating and simplified material laws, this combined methodology provides a physics-based foundation for interpreting spalling mechanisms and can be extended to large-scale elements to support performance-based fire design of concrete structures.

REFERENCES

1. Maluk, C., Tignard, J., Ridout, A., Clarke, T., & Winterberg, R. (2021). Experimental study on the fire behaviour of fibre reinforced concrete used in tunnel applications. Fire Safety Journal, 120, 103173.
2. Hua, N., Khorasani, N. E., Tessari, A., & Ranade, R. (2022). Experimental study of fire damage to reinforced concrete tunnel slabs. Fire safety journal, 127, 103504.
3. Alhawat, H., Hamid, R., Baharom, S., Azmi, M. R., & Kaish, A. B. M. A. (2021). Thermal behaviour of unloaded concrete tunnel lining through an innovative large-scale tunnel fire experimental testing setup. Construction and Building Materials, 283, 122718.
4. Lottman, B. B. G. (2017). The spalling mechanism of fire exposed concrete. Delft University of Technology.
5. Kalifa, P., Menneteau, F. D., & Quenard, D. (2000). Spalling and pore pressure in HPC at high temperatures. Cement and concrete research, 30(12), 1915-1927.
6. Gawin, D., Pesavento, F., & Castells, A. G. (2018). On reliable predicting risk and nature of thermal spalling in heated concrete. Archives of civil and mechanical engineering, 18(4), 1219-1227.
7. Hua, N., Elhami-Khorasani, N., & Tessari, A. (2021). Review of tunnel fire damage assessment methods and techniques. Transportation research record, 2675(5), 279-290.
8. Hua, N., Tessari, A., & Khorasani, N. E. (2021). Characterizing damage to a concrete liner during a tunnel fire. Tunnelling and Underground Space Technology, 109, 103761.
9. Bažant, Z. P., Chern, J. C., & Thonguthai, W. (1982). Finite element program for moisture and heat transfer in heated concrete. Nuclear Engineering and Design, 68, 61-70.
10. Gawin, D., Pesavento, F., Schrefler, B.A.: Modelling of hygro-thermal behavior of concrete at high temperature with thermochemical and mechanical material degradation. Comput. Methods Appl. Mech. Eng. 192, 1731–1771 (2003).
11. Li, R.T., Li, X.K.: A coupled chemo-elastoplastic-damage constitutive model for plain concrete subjected to high temperature. Int. J. Damage Mech 19, 971–1000 (2010).
12. Silling, S.A.: Reformulation of elasticity theory for discontinuities and long-range forces. J. Mech. Phys. Solids 48, 175–209 (2000).
13. S. Oterkus, Peridynamics for the solution of Multi-physics problems, PhD Thesis. University of Arizona, (2015)
14. Oterkus, S., Madenci, E.: Fully coupled poroelastic peridynamic formulation for fluid- filled fractures. Eng. Geol. 225, 19–28, (2017)
15. Zhang, J., Yu, M., Chu, X., & Li, R. (2024). A coupled hygro-thermo-mechanical Cosserat peridynamic modelling of fire-induced concrete fracture: J. Zhang et al. Acta Mechanica, 235(6), 3799-3829.
16. Madenci, E., & Oterkus, E. (2013). Peridynamic theory. In Peridynamic theory and its applications (pp. 19-43). New York, NY: Springer New York.
17. Poon, C. S., Shui, Z. H., & Lam, L. (2004). Compressive behavior of fibre reinforced high-performance concrete subjected to elevated temperatures. Cement and concrete Research, 34(12), 2215-2222.